

Solar farside magnetograms from deep learning analysis of STEREO/EUVI data

Taeyoung Kim^{1,7}, Eunsu Park^{1,7}, Harim Lee^{1,2,7}, Yong-Jae Moon^{1,2*}, Sung-Ho Bae³,
Daye Lim¹, Soojeong Jang⁴, Lokwon Kim³, Il-Hyun Cho^{1,2}, Myungjin Choi⁵ and Kyung-Suk Cho^{4,6}

Solar magnetograms are important for studying solar activity and predicting space weather disturbances¹. Farside magnetograms can be constructed from local helioseismology without any farside data^{2–4}, but their quality is lower than that of typical frontside magnetograms. Here we generate farside solar magnetograms from STEREO/Extreme UltraViolet Imager (EUVI) 304-Å images using a deep learning model based on conditional generative adversarial networks (cGANs). We train the model using pairs of Solar Dynamics Observatory (SDO)/Atmospheric Imaging Assembly (AIA) 304-Å images and SDO/Helioseismic and Magnetic Imager (HMI) magnetograms taken from 2011 to 2017 except for September and October each year. We evaluate the model by comparing pairs of SDO/HMI magnetograms and cGAN-generated magnetograms in September and October. Our method successfully generates frontside solar magnetograms from SDO/AIA 304-Å images and these are similar to those of the SDO/HMI, with Hale-patterned active regions being well replicated. Thus we can monitor the temporal evolution of magnetic fields from the farside to the frontside of the Sun using SDO/HMI and farside magnetograms generated by our model when farside extreme-ultraviolet data are available. This study presents an application of image-to-image translation based on cGANs to scientific data.

Here we apply a deep learning model based on cGANs^{5,6} to solar magnetograms and extreme-ultraviolet images. For training and evaluation datasets, we consider pairs of SDO/AIA⁸ 304-Å images and SDO/HMI⁹ line-of-sight magnetograms with 12-hour cadence from 2011 to 2017. As a result, we produce 4,972 pairs of SDO/AIA images and SDO/HMI magnetograms. We select 4,147 pairs from 2011 to 2017 (except for September and October) for the training dataset and 825 pairs from September and October for the evaluation dataset.

Next we evaluate how well our model generates magnetograms. Figure 1 shows AIA images as the input data, artificial intelligence (AI)-generated magnetograms, and HMI magnetograms. A comparison shows that the bipolar structures of the HMI magnetograms were well restored. The quality of the AI-generated magnetograms is highly comparable with that of the HMI ones. Even though we do not have any a priori conditions, bipolar structures in AI-generated magnetograms mostly follow Hale's law, which is an observational rule: one polarity should precede the other polarity in the northern hemisphere and vice versa in the southern hemisphere. In the

training step, the generator is trained to learn the polarity patterns of active regions. In the evaluation and generation step, the generator reproduces the pattern. Since all data are from the 24th solar cycle, there is no difficulty in producing the Hale's law pattern in this cycle. We note that the polarity of the solar magnetic field is reversed cycle by cycle. Hence, since our model has been trained on the 24th solar cycle, it would be effective for even solar cycles, but should be tested for odd cycles. A careful comparison between two magnetograms shows that the tilt angle between a preceding sunspot and the one that follows it is not always properly generated, which is a limitation of our method. The extreme-ultraviolet 304-Å emission is from the chromosphere-transition region, whereas the HMI measures the magnetic field in the photosphere. The discrepancy in the detailed structures between the real magnetogram and the AI-generated magnetogram reflects the difficulty of the present model in precisely reconstructing the photospheric magnetic fields from chromosphere emission signatures.

Here we also quantitatively evaluate our model for full disk, active regions and quiet regions. Table 1 shows the results of four types of objective measure between SDO/HMI magnetograms and AI-generated ones for three regions. The first objective measurement is the correlation coefficient (CC) between the total unsigned magnetic flux (TUMF) of HMI magnetograms and that of AI-generated ones. Our model shows that the correlation coefficients are 0.97, 0.95 and 0.74 for the full disk, active regions and quiet regions, respectively. These values demonstrate that the generation of the TUMF through deep learning is consistent. The second objective measurement is the pixel-to-pixel correlation between SDO/HMI magnetograms (signed) and AI-generated ones after 8×8 binning. The average correlation coefficients are 0.77 for 825 full-disk images, 0.66 for 1,033 active regions, and 0.21 for 825 quiet regions. These imply that AI-generated magnetograms are well generated for active regions but not for quiet regions. The third objective measurement is the relative error (R1) of the TUMF. The mean R1 values are 0.067, 0.072 and 0.091, and the standard deviation values are 0.036, 0.019 and 0.075 for the full disk, active regions and quiet regions, respectively. This means that our model tends to slightly overestimate the TUMF. The last objective measurement is the normalized mean square error (R2) of the magnetic field. The mean R2 values are 0.053, 0.125 and 0.041, and the standard deviation values are 0.008, 0.049 and 0.005 for the full disk, active regions and quiet regions, respectively, implying that overall there are differences of about 23%, about 35% and about 20% between them.

¹School of Space Research, Kyung Hee University, Yongin, South Korea. ²Department of Astronomy and Space Science, College of Applied Science, Kyung Hee University, Yongin, South Korea. ³Department of Computer Science and Engineering, College of Electronics and Information, Kyung Hee University, Yongin, South Korea. ⁴Space Science Division, Korea Astronomy and Space Science Institute, Daejeon, South Korea. ⁵InSpace Co., Ltd., Daejeon, South Korea. ⁶Department of Astronomy and Space Science, University of Science and Technology, Daejeon, South Korea. ⁷These authors contributed equally: Taeyoung Kim, Eunsu Park, Harim Lee. *e-mail: moonyj@khu.ac.kr

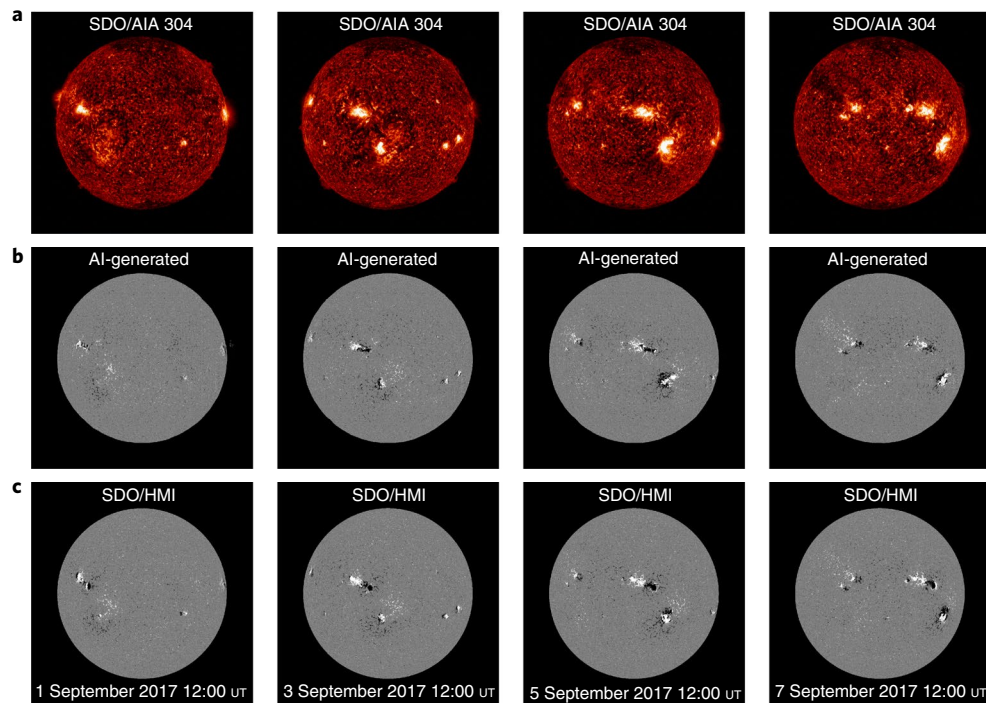


Fig. 1 | Comparison between HMI magnetograms and AI-generated ones from SDO/AIA 304-Å images. **a**, The AIA images, which are the input data for the generator, taken from 1 September to 7 September 2017 with 2-day cadence. **b**, The AI-generated magnetograms from AIA images using the model. **c**, The HMI images are the ground truth. We use ± 100 G as the saturation value for both SDO/HMI magnetograms and AI-generated magnetograms to show the structure of the active regions.

Table 1 | Four objective measures of comparison between SDO/HMI magnetograms and AI-generated ones for full disk, active regions and quiet regions

| | | Full disk | Active region | Quiet region |
|---|--------------------|---|--|--|
| | | 825 images ($1,024 \times 1,024$ pixels) | 1,033 patches (128×128 pixels) | 825 patches (128×128 pixels) |
| Total unsigned magnetic flux CC | | 0.97 | 0.95 | 0.74 |
| Pixel-to-pixel CC (8×8 binning) | | 0.77 | 0.66 | 0.21 |
| Relative error, $R1$ | Mean | 0.067 | 0.072 | 0.091 |
| | Standard deviation | 0.036 | 0.019 | 0.075 |
| Normalized mean square error, $R2$ | Mean | 0.053 | 0.125 | 0.041 |
| | Standard deviation | 0.008 | 0.049 | 0.005 |

Now we apply our model to the EUVI¹⁰ 304-Å images on board the Solar Terrestrial Relationship Observatory (STEREO¹¹), whose filter response function is consistent with that of AIA images^{12–14}, in order to generate farside magnetograms. In the case of STEREO-B, the data are only available before 1 October 2014, owing to multiple hardware anomalies affecting control of the spacecraft orientation. Figure 2 shows a series of extreme-ultraviolet 304-Å images from STEREO-B/EUVI and AIA, and magnetograms from 4 June to 13 June 2014: two farside magnetograms generated by our model and two HMI ones. On 4 June, the STEREO-B is located -164 heliographic longitudinal degrees from the central meridian, which makes the STEREO-B images mostly farside ones. It is evident that the parallel bipolar structures in the NOAA active region 12087, as indicated by the yellow box in Fig. 2, are well generated and conserved during the time of observations. Thus, we can successfully monitor the temporal evolution of this active region from the farside to the frontside of the Sun when farside extreme-ultraviolet data are available.

It is interesting to monitor the continuous evolution of active regions from the farside to the frontside. Figure 3 shows the temporal evolution of the TUMF of the NOAA active region 12087 from 3 June to 19 June 2014. As seen in the figure, the magnetic fluxes of this active region taken from the farside are about two times larger than those from the frontside. We note that the measurements of magnetic fluxes near the eastern limb are substantially underestimated because of the projection effects. The temporal evolution is valuable for space weather forecasts because there were three consecutive strong flares (X2.2, X1.5 and X1.0) near the limb on 10–11 June 2014. We estimate the uncertainty of magnetic flux from farside magnetograms. It is not easy to conduct an inter-calibration between AIA and EUVI given that they could not observe the same field of view. To estimate the uncertainty, we compare one monthly average intensity from two instruments in June 2014, taking into account the solar rotation rate of 13.2° per day. The comparison shows that the EUVI intensity is about 25.5% higher than that of AIA. As seen in Table 1, the magnetic

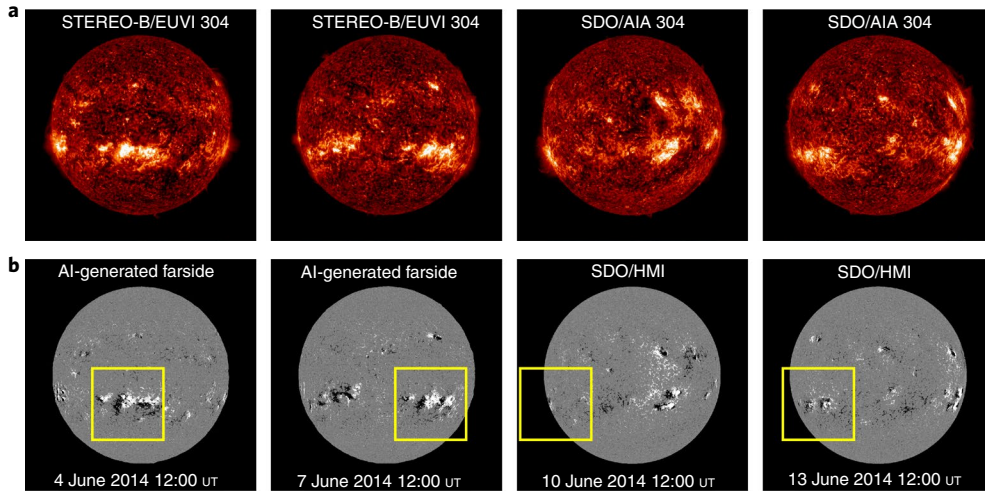


Fig. 2 | A series of 304-Å images and magnetograms. **a**, The first two 304-Å images are taken from STEREO-B/EUVI and the last two from SDO/AIA. **b**, The first two magnetograms are AI-generated farside ones from the model and the last two are taken from SDO/HMI. The yellow boxes show the tracking of the NOAA active region 12087 from the farside to the frontside. We use ± 100 G as the saturation value for both SDO/HMI and AI-generated magnetograms.

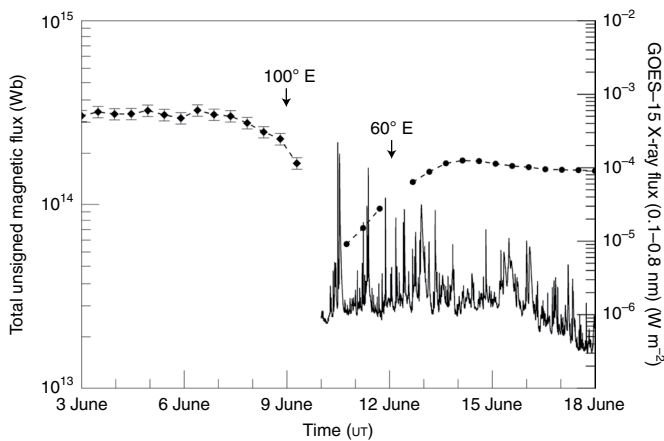


Fig. 3 | A temporal evolution of total unsigned magnetic flux of the NOAA active region 12087 from 3 to 19 June 2014. The filled diamonds represent the total unsigned magnetic flux from AI-generated magnetograms using STEREO-B/EUVI 304-Å images. The error bars indicate their relative error described in Table 1. The downward arrows indicate that the NOAA active region 12087 is located at eastward 60° and 100° heliographic longitudes from the central meridian, respectively. The filled circle represents the total unsigned magnetic flux from SDO/HMI magnetograms. The solid line represents 5-min-averaged GOES-15 X-ray flux (0.1–0.8 nm). GOES, Geostationary Operational Environmental Satellite.

flux is slightly overestimated by about 6.7%. By assuming that the two types of errors are independent, we conjecture that the total uncertainty is an overestimation of 26.3%. As shown in Fig. 3, the magnetic fluxes of the farside magnetograms are about two times larger than those of HMI, which are about four times higher than 26.3%. Thus we conclude that the magnetic flux of this active region greatly decreased from the farside to the frontside of the Sun. Under conditions where extreme-ultraviolet farside data are available, farside magnetograms can be well reproduced, greatly improving current knowledge of the magnetic structure of farside active regions. Our method is reliable if the farside active regions conform to Hale's law, as long as the slight overestimation of their total flux and a possible slight difference in their tilt angle are considered.

In this Letter, the proposed model shows sufficient potential for image-to-image translation between two different scientific sensor images. In the fields of astronomy and geophysics, many multi-wavelength observations are available, so the model can be used to extend these kinds of data. This method can also be applied to a variety of scientific fields that use different kinds of sensor image.

Methods

The use of generative adversarial networks, a popular deep learning method, has been widely examined for image-generation tasks. Isola *et al.*⁶ suggested a general-purpose way to resolve image-to-image translation problems using cGANs. A comparison between output images from the model and the ground truth shows that this model works for various types of image-to-image translations. In this Letter we adopt their model for the image translation of solar magnetograms from SDO/AIA images.

Datasets. We use SDO datasets from the Joint Science Operations Center and STEREO datasets from the STEREO Science Center using SunPy and Solar Software. We first made Level 1.5 images by calibrating, rotating and centring the images, and then converted them to 8-bit scale images of 1,024 by 1,024 pixels. Then we excluded a set of image pairs with poor quality; for example, images too noisy because of solar flares, those with incorrect header information, and images untypical for reasons such as the eclipse of a planet.

Training. The model trains the generator network and the discriminator network with three objectives. The first objective is to train the generator network to minimize the mean error between an HMI magnetogram (I_H) and an AI-generated magnetogram (\hat{I}_H), which is generated using the corresponding AIA image (I_A). The second objective is to train the generator network to reproduce the true data distribution of HMI magnetograms (I_H) from the corresponding AIA images (I_A). The third objective is to train the discriminator network to distinguish the real pair (I_A, I_H) from the AI-generated pair (I_A, \hat{I}_H). In every epoch, one generator network is constructed. Here, one epoch is complete when an entire training dataset of 4,147 pairs has passed through the model for training. As a result, we acquire 120 generator networks while the generator network and the discriminator network are alternately trained for 500,000 iterations (about 120 epochs). For specific hyperparameters, 120 epochs correspond to three days, which is the maximum period that we can compute with our computing capability.

Evaluation. In the evaluation step, we compare the HMI magnetograms with the ones generated using AIA images. For comparison, we estimate the correlation between TUMFs from both magnetograms. Then we compute the relative error, the normalized root-mean-square error, and pixel-to-pixel correlations for all evaluation datasets. When we calculate the TUMFs of both magnetograms, we use 10 G as a threshold to consider the noise level of line-of-sight SDO/HMI magnetograms¹⁵. The equation for the relative error ($R1_i$) of the TUMF (Φ_i) is given by

$$R1_i = (\Phi_i^{\text{AI}} - \Phi_i^{\text{HMI}}) / \Phi_i^{\text{HMI}} \quad (1)$$

where i is the serial number of the 825 evaluation samples. This value corresponds to the overestimation ($R1_i > 0$) or underestimation ($R1_i < 0$) that our method attributes to the TUMF. The equation for the normalized mean square error ($R2_i$) of the magnetic field (B_i) is given by

$$R2_i = \sum (B_j^{AI} - B_j^{HMI})^2 / \sum (B_j^{HMI})^2 \quad (2)$$

where i is the serial number of the 825 evaluation samples and j is the pixel number of the solar disk. In addition, we did the same analysis for cropped patches of active and quiet regions within $\pm 60^\circ$ of the central meridian.

Data availability

The code is available at <https://github.com/tykimos/SolarMagGAN>. In the readme file, we explain the architecture and selected hyperparameters. The SDO data are available from the SDO data centre (<https://sdo.gsfc.nasa.gov/data/>), the Joint Science Operations Center (<http://jsoc.stanford.edu/>) and the Korean Data Center for SDO (<http://sdo.kasi.re.kr/>). The STEREO data are available from the STEREO Science Center (<https://stereo-ssc.nascom.nasa.gov/data.shtml>). We used the following open-source packages: NumPy (<http://www.numpy.org>) and Keras (<https://keras.io/>).

Received: 10 April 2018; Accepted: 24 January 2019;

Published online: 04 March 2019

References

- Solanki, S. K., Inhester, B. & Schussler, M. The solar magnetic field. *Rep. Prog. Phys.* **69**, 563–668 (2006).
- Lindsey, C. & Braun, D. C. Seismic images of the far side of the Sun. *Science* **287**, 1799–1801 (2000).
- Braun, D. C. & Lindsey, C. Seismic imaging of the far hemisphere of the Sun. *Astrophys. J. Lett.* **560**, 189–192 (2001).
- Lindsey, C. & Braun, D. C. Seismic imaging of the Sun's far hemisphere and its applications in space weather forecasting. *Space Weather* **15**, 761–781 (2017).
- Goodfellow, I. et al. Generative adversarial nets. *Adv. Neur.* **2014**, 2672–2680 (2014).
- Isola, P., Zhu, J.-Y., Zhou, T. & Efros, A. A. Image-to-image translation with conditional adversarial networks. *IEEE Proc. Comput. Vision Pattern Recog.* **2017**, 1125–1134 (2017).
- Pesnell, W. D., Thompson, B. J. & Chamberlin, P. C. The Solar Dynamics Observatory (SDO). *Sol. Phys.* **275**, 3–15 (2012).
- Lemen, J. R. et al. The Atmospheric Imaging Assembly (AIA) on the Solar Dynamics Observatory (SDO). *Sol. Phys.* **275**, 17–40 (2012).
- Schou, J. et al. Design and ground calibration of the Helioseismic and Magnetic Imager (HMI) instrument on the Solar Dynamics Observatory (SDO). *Sol. Phys.* **275**, 229–259 (2012).
- Howard, R. A. et al. Sun Earth Connection Coronal and Heliospheric Investigation (SECCHI). *Space Sci. Rev.* **136**, 67–115 (2008).
- Kaiser, M. L. et al. The STEREO mission: an introduction. *Space Sci. Rev.* **136**, 5–16 (2008).
- Dere, K. P. et al. CHIANTI atomic database for emission lines. *Astron. Astrophys. Suppl.* **125**, 149–173 (1997).
- Landi, E., Zanna, G. D., Young, P. R., Dere, K. P. & Mason, H. E. CHIANTI—an atomic database for emission lines. XII. Version 7 of the database. *Astrophys. J.* **744**, 99–107 (2012).
- Nitta, N. V. et al. Soft X-ray fluxes of major flares far behind the limb as estimated using STEREO EUV images. *Sol. Phys.* **288**, 241–254 (2013).
- Liu, Y. et al. Comparison of line-of-sight magnetograms taken by the Solar Dynamics Observatory/Helioseismic and Magnetic Imager and Solar and Heliospheric Observatory/Michelson Doppler Imager. *Sol. Phys.* **279**, 295–316 (2012).

Acknowledgements

We thank the numerous team members who contributed to the success of the SDO mission, as well as the STEREO mission. We acknowledge the community efforts devoted to developing the open-source packages that were used in this work (NumPy and Keras). This work was supported by the BK21+ Program through the National Research Foundation (NRF) funded by the Ministry of Education of Korea, the Basic Science Research Program through the NRF funded by the Ministry of Education (NRF-2016R1A2B4013131), a grant from the NRF funded by the Korean government (number NRF-2013M1A3A3A02042232), the Korea Astronomy and Space Science Institute under the R&D programme supervised by the Ministry of Science and ICT, the Korea Astronomy and Space Science Institute under the R&D programme 'Development of a Solar Coronagraph on International Space Station (Project No. 2019-1-850-02)' supervised by the Ministry of Science and ICT, a grant from the Institute for Information & Communications Technology Promotion (IITP) funded by the Korea government (MSIP) (number 2018-0-01422, 'Study on Analysis and Prediction Technique of Solar Flares'), and the Artificial Intelligence Laboratory at the InSpace Co., Ltd. The SDO data were (partly) provided by the Korea Data Center (KDC) for SDO in cooperation with NASA and the SDO/HMI Team, which is operated by the KASI.

Author contributions

T.K., E.P. and H.L. contributed equally to this study. T.K., E.P., H.L. and Y.-J.M. devised the method, analysed data and wrote the manuscript. S.-H.B. participated in discussing the results and contributed to improving the methodology. D.L., S.J., I.-H.C., L.K., M.C. and K.-S.C. participated in discussing the results.

Competing interests

The authors declare no competing interests.

Additional information

Reprints and permissions information is available at www.nature.com/reprints.

Correspondence and requests for materials should be addressed to Y.-J.M.

Publisher's note: Springer Nature remains neutral with regard to jurisdictional claims in published maps and institutional affiliations.

© The Author(s), under exclusive licence to Springer Nature Limited 2019